ELSEVIER

Journal of Fluids and Structures 24 (2008) 576–588

JOURNAL OF FLUIDS AND STRUCTURES

www.elsevier.com/locate/jfs

Droplet formation from a pulsed vibrating micro-nozzle

G. Yang, J.A. Liburdy*

Department of Mechanical Engineering, Oregon State University, Corvallis, OR 97331, USA

Received 12 July 2006; accepted 21 October 2007
Available online 4 March 2008

Abstract

Micro-droplet formation from a passive vibrating micro-nozzle driven by a pulsed pressure wave is numerically simulated. The micro-nozzle is formed from an orifice in a thin walled plate that is allowed to freely vibrate due to the pressure loading on the plate. The analysis couples the fluid flow from the nozzle and the resultant droplet formation with the nozzle vibration calculated using large deflection theory. The problem is made nondimensional based on the capillary parameters of time, velocity and pressure. The applied pressure and nozzle material properties are varied to alter the vibration characteristics of the orifice plate used to form the nozzle. The initiation of drop formation is found to coincide with a threshold impulse input, defined as the product of the pressure magnitude and the pulse duration. Increasing the impulse can result in multiple satellite droplet formation, but the effect on the primary droplet size is minor. The vibration of the nozzle only weakly influences the droplet break-off time, but is shown to significantly affect the droplet volume, shape, and satellite droplet formation.

Keywords: Droplet formation; Vibration; Numerical simulation

1. Introduction

Micro-droplet formation for drop-on-demand applications based on rigid chamber designs has been studied for many years, for instance, see the early works Fromm (1982), Bogy and Talke (1984), and Shield et al. (1987). This general area has wide applications that include ink-jet printing, pharmaceutical dispensing, three-dimensional rapid prototype modeling, and others. Recently, there has developed growing needs to improve the control of parameters such as micro-droplet velocity and size, rate of droplet production and satellite formation. Some design options have been proposed in the recent past that involves active control of the driving forces required to form drops. For example, Kamisuki et al. (1998, 2000) described a micro-electro-mechanical diaphragm drop ejector, and experimentally characterized the droplet formation based on this design. Pan et al. (2002) numerically simulated the droplet formation process from this same design using commercially available software. This device is based on a rigid nozzle, driven by a piezoelectric actuated diaphragm. Percin and Khuri-Yakub (2003) proposed a design based on an open reservoir coupled with an actively vibrating nozzle plate driven by a piezoelectric stack.

*Corresponding author. Tel.: +1 541 737 7017; fax: +1 541 737 2600.
E-mail address: liburdy@engr.oregonstate.edu (J.A. Liburdy).

0889-9746/$ - see front matter © 2007 Elsevier Ltd. All rights reserved.
doi:10.1016/j.jfluidstructs.2007.10.012

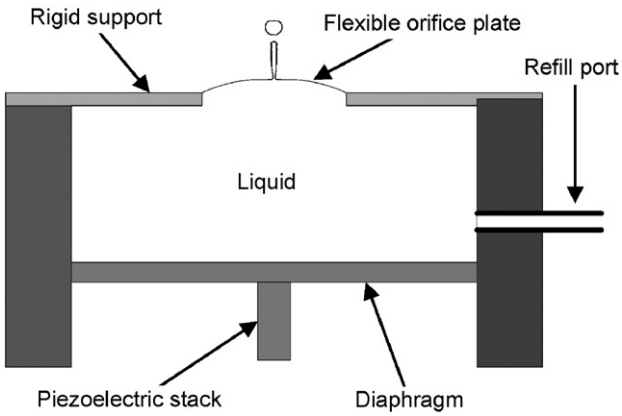

Fig. 1. Schematic of a concept drop ejector device with a flexible nozzle orifice plate bounding a liquid reservoir which is driven by a piezoelectric actuated diaphragm; figure is not to scale.

This study investigates the case of a naturally vibrating orifice micro-nozzle plate during micro-droplet formation. Rather than drive the plate actively, the pressure wave used to form the droplet is used to set the plate in a specific vibration mode. The modal response depends on the plate material, its geometry and the particular input pressure wave. The concept behind the use of a flexible nozzle is shown schematically in Fig. 1. The device consists of a rigid chamber that supplies fluid through a refill port, a piezoelectric crystal stack which can drive a diaphragm at a prescribed displacement pulse, and a flexible orifice plate which deflects based on the pressure within the fluid reservoir. The orifice plate is expected to be very thin, on the order of, or less than, the orifice diameter (which is taken here as 50 μm). The deflection of the plate will depend on the thickness, Young's modulus of the material used to form the plate and how the plate is attached, or the edge boundary condition. In this study it is assumed that the plate edge is rigidly attached to the stiff support forming the top boundary of the reservoir. In general, the plate deflection will be influenced by the fluid structure interaction between the driving diaphragm, fluid reservoir and orifice plate. In this simulation we apply a uniform pressure pulse at the bottom of the orifice plate and calculate the plate deflection, taking into account the circular hole in the plate. This deflection is assumed to be independent of the micro-droplet formation process since the volume of a droplet is insignificant compared to the volume of fluid in the reservoir.

A one-dimensional (1-D) model, restricted to axisymmetric and irrotational flow, for droplet formation has been used very successfully by a number of previous researchers Adams and Roy (1986), Shield and Bogy (1986), Yamamoto et al. (1991), and Eggers and Dupont (1994). Ambravaneswaran et al. (2002) compared one- and two-dimensional (2-D) models for axisymmetric gravity driven droplet formation. Their study shows that the difference between a 1-D model and a 2-D model is small, within a few percent, when the surface tension force dominates the flow. The primary limitation of the use of a 1-D model is the lack of its ability to account for the "overturn" or "backflow" phenomena. This condition may occur during micro-drop formation when the shape of the leading portion of the filament causes the fluid near the side edges of the drop to lag behind the leading edge in such a way as to cause the surface location to have multiple radial values at any given axial location along the filament. Eggers (1993) studied the break-off phenomenon showing that close to break-off the solution follows a universal exponential form. Day et al. (1998) studied the break-off shape of inviscid fluid finding that the break-off has unique shapes with two cones of angles of 18.1° and 112.8°. Chen et al. (2002) show for water that "overturn" occurs at a minimum radius of 1.3% of the nozzle radius.

The 1-D model in this study accounts for flow through a thin walled orifice nozzle with a time dependent deflection based on the orifice plate motion. The nozzle vibration is modeled using large deflection theory of thin plates. Large plate deflection theory, based on the energy method, has been used by Roman and Aubry (2003) to predict defections in micro-scale synthetic jets. In the synthetic jet, flow is not through the deflecting plate, as in the current study, but is used to drive flow through a cavity and then through a rigid tube, or fixed nozzle. The deflection analysis used by Roman and Aubry determines the total volume deflection and does not include local time dependent deflections. In the current study, time dependent nozzle deflection is used to predict droplet formation that is then compared to the droplet formation from the identical geometry using a perfectly rigid orifice plate. Table 1 lists the dimensional parameters of the problem studied. Note that the fluid properties are taken to be those of water, except in those cases where the viscosity is varied.

Table 1
Geometric and fluid parameters

Orifice nozzle radius, a (μm)	50
Nozzle plate radius, r_p (μm)	4000
Nozzle plate thickness, h (μm)	16
Density of plate, ρ_p (kg/m^3)	7590
Plate Young's modulus, E (GPa)	25.5, 102, 408
Density of fluid, ρ (kg/m^3)	998.2
Air-fluid interface surface tension, σ (kg/s^2)	0.0728
Fluid dynamic viscosity, μ (kg/m s^2)	10^{-3}–1.2×10^{-2}

Table 2
Capillary scales based on parameters in Table 1

Length scale, l_c (μm)	50
Time scale, t_c (μs)	41.40
Velocity scale, u_c (m/s)	1.208
Pressure scale, P_c (Pa)	1456
Impulse scale, M_c (N s/m^2)	0.060

2. Mathematical model

The governing equations of the current problem consist of the conservation equations for the fluid flow model and the nozzle plate deflection. The 1-D fluid flow equations are written using a coordinate frame moving with the same speed as the nozzle, with the origin fixed at the vibrating nozzle exit plane. Therefore, the equations are written in terms of an accelerating frame of reference. Results are then converted back to a stationary reference frame. The equations are made nondimensional using the capillary scales, which are based on the nozzle radius, a, and relevant fluid properties: the density, ρ, and surface tension, σ. The capillary length scale, $l_c = a$; the capillary velocity scale, $u_c = (\sigma/\rho a)^{1/2}$; the capillary time scale, $t_c = (\rho a^3/\sigma)^{1/3}$; and the capillary pressure scale, $p_c = \sigma/a$. Based on the dimensional parameters used in this study, provided in Table 1, the associated capillary scales are given in Table 2.

Under the assumption that the fluid is incompressible, Newtonian and the gravitational effects are negligible, the nondimensional conservation of mass and Navier–Stokes equations become, respectively:

$$\frac{Dr^*}{Dt^*} + \frac{r^*}{2}\frac{\partial u^*}{\partial \eta^*} = 0, \tag{1}$$

$$\frac{Du^*}{Dt^*} = -\left[\frac{\partial}{\partial \eta^*}\left(\frac{1}{K_N^*} + \frac{1}{K_T^*}\right) - 3\mathrm{Oh}\frac{1}{r^{*2}}\frac{\partial}{\partial \eta^*}\left(r^{*2}\frac{\partial u^*}{\partial \eta^*}\right)\right] - \frac{\mathrm{d}u_o^*}{\mathrm{d}t^*}, \tag{2}$$

where t is the time, η is the axial position measured from the nozzle exit, u is the axial fluid velocity, r is the local radius of the fluid filament, u_o is the orifice plate velocity at the edge of the orifice, and $\mathrm{Oh} = \mu/(\rho a\sigma)^{1/2}$ is the capillary Ohnesorge number, with μ the fluid dynamic viscosity. K_N and K_T are the local principal radii of the fluid stream, normal and tangential to the axial direction, respectively, which are given by Middleman (1995), and in nondimensional form are

$$K_N^* = r^*\sqrt{1 + \left(\frac{\partial r^*}{\partial \eta^*}\right)^2}, \quad K_T^* = \frac{-\sqrt{(1 + (\partial r^*/\partial \eta^*)^2)^3}}{(\partial^2 r^*/\partial \eta^{*2})}. \tag{3}$$

To complete the model the boundary conditions are given as follows. For the 1-D model the boundaries consist of the free moving surfaces of both the droplet and trailing filament (after droplet break-off), and the nozzle exit plane (when the filament is attached to the nozzle). The velocity at the free surface front and rear tip is estimated to be equal to the neighboring node velocity inside the fluid filament. Therefore, when the fluid has a free surface, with $r = 0$ then $u_{i-1} = u_i$ for the rear tip and $u_{i+1} = u_i$ for the leading tip, where u_i is the velocity of the node one element within the filament from either the rear or leading tip.

At the nozzle exit plane, the fluid velocity is determined from a momentum balance of the flow leaving the reservoir, where the filament radius is identical to the nozzle radius. The conditions at the nozzle exit plane are $\eta = 0$: $r = 1$ and $u = u_e$. The time variation of u_e is determined based on a pressure driven flow from a large reservoir that has negligible momentum. The flow exits through a small diameter, square edged orifice. A simplified momentum balance through the orifice yields the following relationship, assuming the flow acceleration is dominated by the pressure drop across the orifice:

$$\frac{\mathrm{d}u_e^*}{\mathrm{d}t^*} = \frac{p_o^* - p_e^*}{h^*}, \tag{4}$$

where p_o^* is the driving pressure in the reservoir, p_e^* is the liquid pressure at the nozzle exit plane, and h^* is the plate thickness. The reservoir pressure is provided from the imposed time dependent step function, mentioned previously. The exit plane pressure varies with time due to the local curvature of the surface of the evolving liquid filament, which is based on the surface tension. Based on this, the exit pressure p_e^* is calculated using Young–Laplace equation, (Middleman, 1995) using the time variation of the surface curvature.

The governing equation for the deflection of the orifice plate is based on large deflection theory for a thin plate, assuming axisymmetric conditions. The deflection, w, given by Szilard (1974), written in nondimensional form, is

$$D^*\nabla^4 w^* + \frac{\rho_p h}{\rho a}\frac{\partial^2 w^*}{\partial t^{*2}} + C\sqrt{\frac{a}{\rho\sigma}}\frac{\partial w^*}{\partial t^*} = h^*\frac{1}{r^*}\frac{\partial}{\partial r^*}\left(\frac{\partial w^*}{\partial r^*}\frac{dF^*}{dr^*}\right) + p^*, \tag{5}$$

where ρ_p is the plate density, C is the vibration damping factor, D is the plate bending rigidity, $D^* = Eh^3/[12(1-\nu^2)\sigma a^2]$, E is Young's modulus and $E^* = Ea/\sigma$, ν is Poisson's ratio, p^* is the driving pressure applied to the reservoir, $p^* = p_o/[\sigma/a]$, and F^* is the nondimensional Airy stress function:

$$\nabla^4 F^* = -\frac{E^*}{r^*}\frac{\mathrm{d}w^*}{\mathrm{d}r^*}\frac{\mathrm{d}^2 w^*}{\mathrm{d}r^{*2}}. \tag{6}$$

The pressure pulse period and the droplet break-off time occurs well within one cycle of the nozzle plate vibration (on the order of 5% of the plate vibration period). Therefore, the plate dynamics of interest are only during the first cycle of the plate vibration. Subsequent damping will occur at later times depending on the damping coefficient, C, but is not of concern for such a long plate vibration period compared with the micro-droplet time scales of droplet formation. Consequently, a small damping factor of 0.05 is used, which has an insignificant effect on the plate vibration during the first cycle.

The boundary conditions for the nozzle plate vibration equations are based on a clamped edge at the plate periphery and a free edge at the orifice edge. The clamped edge boundary condition requires

$$w^*\big|_1 = 0 \quad \text{and} \quad \left.\frac{\partial w^*}{\partial r^*}\right|_1 = 0, \tag{7}$$

and the orifice free edge boundary condition requires

$$\frac{\partial^3 w^*}{\partial r^{*3}} + \frac{1}{r^*}\frac{\partial^2 w^*}{\partial r^{*2}} - \frac{1}{r^{*2}}\frac{\partial w^*}{\partial r^*} = 0 \quad \text{and} \quad \frac{\partial^2 w^*}{\partial r^{*2}} + \frac{u}{r^*}\frac{\partial w^*}{\partial r^*} = 0. \tag{8}$$

The nozzle acceleration, which appears in the fluid momentum equation, Eq. (2), is determined by solving for the plate deflection, w, and then evaluating the acceleration of the edge of the orifice.

Eq. (5) is solved using a modal expansion method given by Soedel (1993). The plate is assumed to vibrate at its natural vibration modes and that for large deflections the nozzle plate vibration is dominated by its first mode. The plate vibration modal shapes are determined from Eq. (5) with the pressure term eliminated and the boundary conditions from Eqs. (7) and (8). The modal expansion method represents the time dependent deflection, $w(r, t)$, as

$$w^*(r^*, t^*) = w_o^*(t^*)\Re(r^*), \tag{9}$$

where $w_o^*(t)$ is the time dependent amplitude and $\Re(r^*)$ is the mode shape function, which is a combination of the plate natural vibration mode shapes. Substituting Eq. (9) into Eqs. (5) and (6), and integrating over the radius, results in

$$\frac{\mathrm{d}u_o^*}{\mathrm{d}t^*} + c_1 E^* h^* \frac{w_o^{*3}}{r_p^{*4}} + c_2 D^* \beta^4 w_o^* + c_2 C\sqrt{\frac{a}{rs}}u_o^* = p^*, \tag{10}$$

where r_p is the nozzle plate radius, β is the mode shape parameter, and c_1 and c_2 are constants determined by the mode shape functions. The value of β is determined by the boundary condition and plate properties where $\beta = 3.19622$ for the first mode shape with a clamped edge boundary condition. The values of c_1 and c_2 are determined by the mode shape

functions by integration along the radius:

$$c_2 = \int \Re(r^*)\,\mathrm{d}r^* \quad \text{and} \quad c_1 = \frac{1}{E^* w_o^* (t^*)^3} \int \frac{1}{r^*} \frac{\partial}{\partial r^*} \left(\frac{\partial \Re(r^*)}{\partial r^*} \frac{\mathrm{d}F^*}{\mathrm{d}r^*} \right),$$

where $\mathrm{d}F^*/\mathrm{d}r^*$ is evaluated by integrating Eq. (6).

In order to simulate the free movement of the droplet and to account for formation of satellite droplets, a droplet break-off criterion is needed. An analytic break-off criteria, or even details of the actual mechanism, has not been fully developed. The process is thought to be driven by a capillary pinching mechanism, which is discussed by Lin (2003). As the filament thins to be on the order of the molecular scale, the physical mechanism becomes very complex. Typically, numerical simulations that have been shown to agree well with experiment, define the break-off criteria based on a minimum radius of the filament. Adams and Roy (1986) used a break-off criterion of the filament radius less than 5% of the nozzle radius. Eggers and Dupont (1994) used a filament radius less than 0.1% of the nozzle radius as the break-off criteria. In this study, the break-off criterion is when the filament reaches 0.1% of the nozzle radius or when "overturn" occurs. The self-similar pinch-off shape shown by Day et al. (1998) is used in defining the primary drop and filament shape near the break-off. When the overturn criteria is used the results presented here are found to be within 0.2% of the break-off times scaled by Chen et al. (2002). Once break-off occurs the droplet and filament shape is determined at the break-off point by setting the radius to zero at the axial location of break-off.

3. Numerical approach

Eqs. (1) and (2) are expressed in integral form as the vector equation

$$X + \int Y\,\mathrm{d}t^* + Z = 0, \tag{11}$$

where

$$X = \begin{Bmatrix} \ln(r^*) \\ u^* \end{Bmatrix}, \qquad Y = \begin{Bmatrix} \dfrac{u^*}{2} \\ \dfrac{\partial}{\partial h^*}\left(\dfrac{1}{K_N^*} + \dfrac{1}{K_T^*}\right) - 3\mathrm{Oh}\dfrac{1}{r^{*2}}\dfrac{\partial}{\partial h^*}\left(r^{*2}\dfrac{\partial u^*}{\partial h^*}\right) \end{Bmatrix} \quad \text{and} \quad Z = \begin{Bmatrix} 0 \\ u_o^* \end{Bmatrix}.$$

Similarly, Eq. (10) is expressed in integral form as the vector equation:

$$U = \int W\,\mathrm{d}t^*, \tag{12}$$

where

$$U = \begin{Bmatrix} w_0^* \\ u_0^* \end{Bmatrix}, \qquad W = \begin{Bmatrix} u_0^* \\ p_0^* - c_1 E^* h^* \dfrac{w_o^{*3}}{r_p^{*4}} - c_2 D^* \beta^4 w_0^* - c_2 C \sqrt{\dfrac{a}{rs}} u_0^* \end{Bmatrix}.$$

The MacCormack scheme was used to numerically integrate the term Y. The nozzle acceleration term, Z, is added at the end of each time step. The nozzle vibration velocity, u_0^*, is obtained by integrating Eq. (12) using a Runga–Kuta method. The nodal positions along the fluid filament are held fixed until the calculation is complete for a given time step, n. Nodal positions are then updated based on the local velocities using a second-order trapezoid differencing scheme. Note that grid size is variable in both space and time throughout the length of the filament. Each grid is allowed to stretch or shrink as necessary to satisfy the conservation relationships of mass and momentum. Also, the grid is adaptive in the sense that, if a grid is stretched/shrunk beyond the nondimensional distance of 0.01/0.00375 (1%/0.375% of the nozzle radius), it is then divided/combined.

The accuracy of the numerical scheme was checked in three ways. First, a grid independent solution was determined based on the evaluation of four primary parameters: the break-off time, the break-off radius, the break-off position, and the volume of the filament after break-off. Successive refinement of the grid showed that the results of these four parameters are within 0.1% when the largest nondimensional grid size was decreased from 0.02 to 0.01. Second, the simulation validity was checked by comparing results at discrete times for a gravity driven droplet formation against the results of Eggers and Dupont (1994) over a series of time steps, shown in Fig. 2. The results of Eggers and Dupont are based on a 2-D model. In addition, the experimental results of Peregrine et al. (1990) for a similar gravitationally

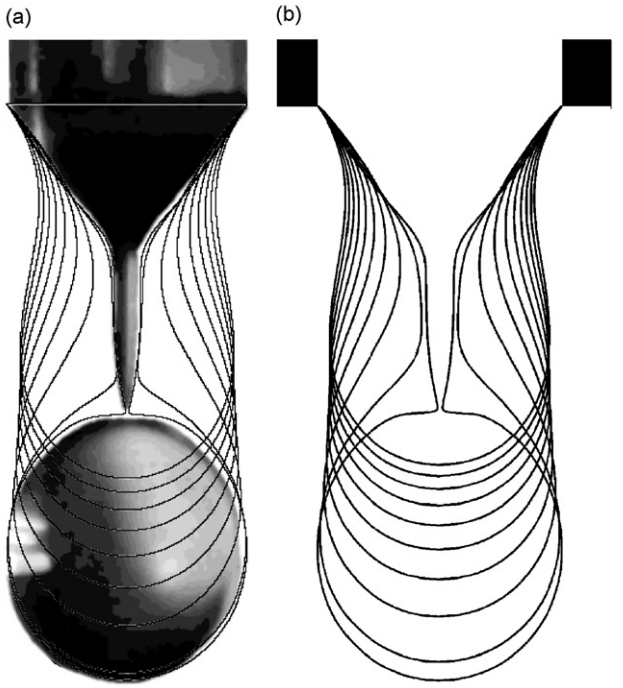

Fig. 2. Present model comparison of the formation of a gravity driven water droplet: (a) experimental results of Peregrine et al. (1990) superimposed over simulation of Eggers and Dupont (1994); (b) results of the present model with line contours at the same relative times as the experiments and previous numerical simulations.

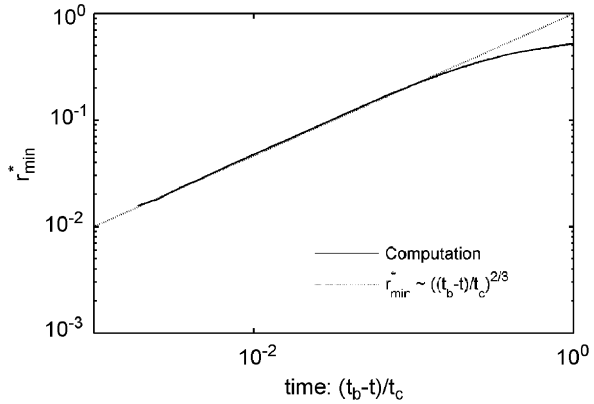

Fig. 3. Variation of the minimum radius prior to break-off versus time to break-off for both the present (solid line) and theory presented by Chen et al. (2002) showing $r^*_{min} \sim ((t-t_b)/t_c)^{2/3}$, results are for the case of water, Oh = 0.0167.

driven droplet formation are superimposed in the figure. The results computed in this study match very well those of Eggers and Dupont and those of Peregrine, well within the level of uncertainty of their results concerning both drop diameter and filament shape.

To further confirm the accuracy of the model and numerical results of the present study, the computed minimum radius as a function of the time to break-off is plotted for the case of water, Oh = 0.06, in Fig. 3. The results agree well with the prediction of Chen et al. (2002) showing that the minimum radius follows the scaling theory, $r^*_{min} \sim ((t-t_b)/t_c)^{2/3}$ for minimum nondimensional radii between 0.015 and 0.2, and that "overturn" occurs at a minimum radius of $r^*_{min} \approx 0.015$ for the applied pressure boundary condition. Based on this, it is concluded that very good accuracy is obtained using the current 1-D simulations.

4. Results and discussion

4.1. Stationary nozzle

As shown by Elrod et al. (1989), the initial impulse per unit area of the driving pressure pulse, defined as $M_i = PT$ is an important parameter for droplet formation from a free liquid surface, where P is the magnitude of the pressure pulse, and T is the duration of the pressure pulse. The impulse associated with the driving pressure pulse required to generate a high-speed micro-droplet is studied first. The critical impulse needed to formulate micro-droplets, M_{cri}, normalized by the impulse based on the capillary scales, M_c, is shown in Fig. 4, versus nondimensional pressure for the case of water, Oh = 0.0167, along with the associated liquid jet shapes at the time of break-off. The results indicate that for increasing pressure the threshold impulse becomes a constant, about 1.05 of the capillary impulse scale. When the pressure magnitude is low, significantly higher impulse input is required for droplet formation, for instance, when the pressure is less than twice the capillary pressure the liquid surface oscillates but there is insufficient momentum for a droplet to form. It should be noted that when impulse values are much greater than the minimam given in the figure, more satellites are formed (Yang, 2003).

The effect of the applied impulse on droplet break-off time is shown in Fig. 5, for the four impulse values studied. The liquid filament shape at the time of droplet break-off is shown in the figure for each pressure magnitude. Results indicate that the primary droplet break-off time is weakly affected by the input impulse. However, satellite droplet break-off times increase with increasing impulse. These longer times are associated with a significantly longer liquid thread attached to the nozzle at the time of the primary droplet break-off. These results can be explained as follows. As the liquid leaves the nozzle, the surface tension forces decelerate the liquid near the exit. Higher impulse values result in high fluid velocities at the end of the pressure pulse; therefore, longer times are required for the fluid to decelerate sufficiently to cause the satellite break-off.

The effect of the impulse on the droplet volume, droplet velocity and satellite volume is given in Table 3. The normalized primary droplet volume increases with the applied impulse. The droplet velocity increases significantly with the impulse, with a corresponding increase in satellite break-off time and satellite volume. The consequence of forming a high-speed micro-droplet is increased potential for satellite formation.

4.2. Vibrating nozzle

The effect of nozzle vibration on micro-droplet formation is presented by comparing results for three vibrating nozzles with different rigidity values to those of a rigid nozzle, all with the same geometry. In these results, the pressure pulse driving the micro-droplet formation is the same for the rigid and vibrating nozzle cases, and is chosen to have an impulse slightly larger than the necessary threshold impulse, shown in Fig. 5, such that excessive satellite formation does not occur. An example of the droplet formation process from a vibrating nozzle is shown in Fig. 6, where the properties are for water, and the plate Young's modulus, E, has a value of 408 GPa. The sequence in the figure is in

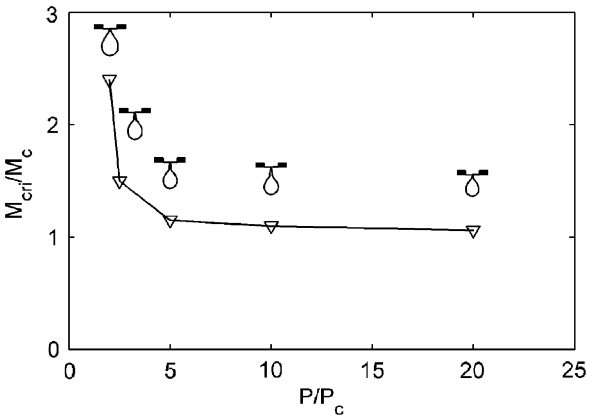

Fig. 4. Critical threshold impulse, M_{cri} for droplet formation versus applied pressure for Oh = 0.0167 and a rigid nozzle, impulse and pressure are nondimensionalized by the capillary impulse, $M_c = P_c t_c$, and capillary pressure, P_c; also included is the droplet shape shown at time of break-off.

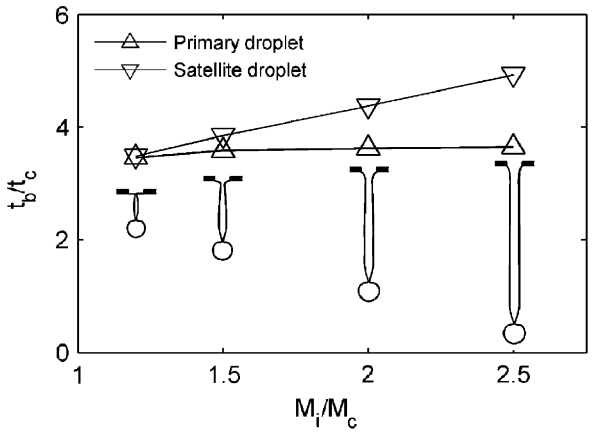

Fig. 5. Nondimensional break-off time versus initial impulse for both primary and satellite droplets for Oh = 0.0167 and a rigid nozzle; filament shape is also shown at the time of the primary droplet break-off.

Table 3
Droplet formation characteristics versus driving impulse; capillary scale for volume is $V_c = (4/3)\rho a^3(\mathrm{m}^3)$

Impulse input, M_i/M_c	Droplet break-off time, t_b/t_c	Droplet volume, V_d/V_c	Droplet velocity, u_d/u_c	Satellite break-off time, t_s/t_c	Satellite droplet volume, V_s/V_c
1.2	3.45	1.43	0.92	3.49	0.22
1.5	3.55	1.85	2.48	3.83	0.59
2	3.57	2.17	4.38	4.40	1.05
2.5	3.64	2.37	6.20	4.90	1.48

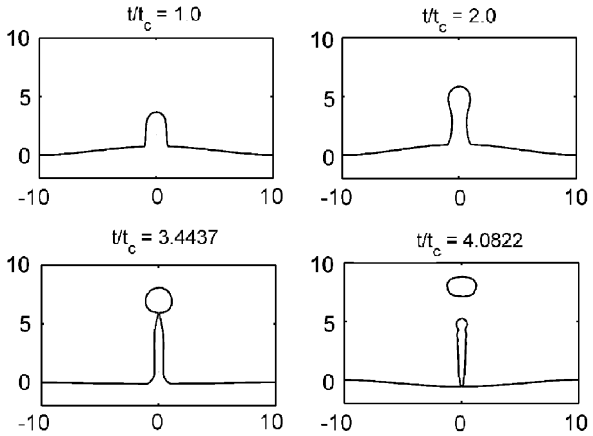

Fig. 6. Typical vibrating nozzle plate break-off sequence at four times up until break-off for Oh = 0.0167, and $E = 408\,\mathrm{GPa}$; the vertical length scale shown is normalized by the nozzle radius.

nondimensional time based on the capillary time scale. The initial state is a flat orifice plate with a slight positive pressure applied to the reservoir to allow the existence of a meniscus at the orifice nozzle exit plane. The pressure pulse is applied at time $t/t_c = 0$. Simultaneously, the orifice plate deflects upward and fluid emerges as a liquid column from the orifice. The initial pinching, or necking, is shown to occur at $t/t_c = 1.0$, where the plate has oscillated through a phase angle of approximately $\pi/2$. The necking continues until break-off occurs, in this case at $t/t_c = 3.4$.

After break-off the primary micro-droplet is formed and the filament is still attached to the vibrating orifice plate. Depending on conditions, as shown later, the filament may eventually break-off, forming one or more satellite droplets. In the following discussion the entire filament is referred to as the satellite, even though it may result in several individual droplets.

For the same input pressure the orifice plate vibration period and amplitude change depending on the material's Young's modulus, E. Results are given for three different Young's modulus values, $E = 25.5$, 102, and 408 GPa, corresponding to low, intermediate, and high rigidity, respectively. The nozzle vibration velocity is shown in Fig. 7 for the applied pressure impulse showing that the nozzle vibration velocity magnitude is dominated by the input pressure impulse. The plate stiffness changes the nozzle vibration frequency, but the magnitude variation is negligible. The initial linear response seen in the figure occurs during the pressure impulse application.

Various characteristics of droplet and satellite formation are given in Figs. 8–12 for the three values of E along with results for the rigid plate. Also, Table 4 contains the nozzle vibration period, peak nozzle displacement, peak nozzle velocity, and the initial nozzle acceleration due to the applied pressure pulse. The initial acceleration of the nozzle is essentially the same for these three nozzles, and the peak nozzle velocity occurs at the end of the pressure pulse. For increasing E, a stiffer plate, both the amplitude and period of the plate vibration decrease. Note, that for all of these cases, the nozzle deflection magnitude is very large compared to the orifice nozzle radius. As given in Table 1, the plate thickness h is 16 μm and the orifice radius is 50 μm; therefore, the peak deflection to plate thickness ratio, w_o/h, varies from approximately 1.5 to 4.7. A consequence of this large deflection of the orifice plate is that there is a non-linear relationship between plate amplitude and frequency.

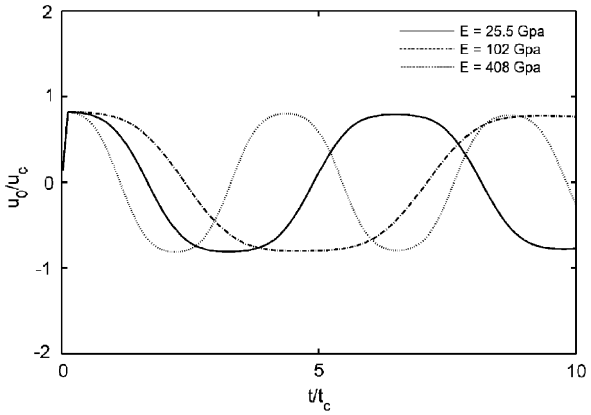

Fig. 7. Time variation of the nozzle vibration velocity for an impulse $M_i/M_c = 1.2$ and three different degrees of stiffness as measured by Young's modulus, E; velocity is nondimensionalized by the capillary velocity.

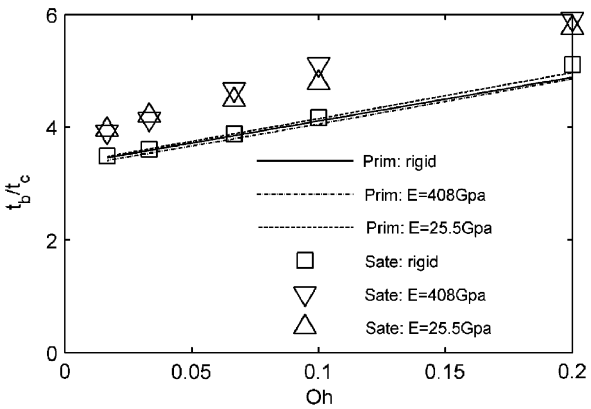

Fig. 8. Variation of primary droplet break-off time (lines) and satellite droplet break-off time (symbols), nondimensionalized by the capillary time scale, versus Oh for a rigid nozzle plate and two flexible plates measured by Young's modulus, E; for all cases $M_i/M_c = 1.2$.

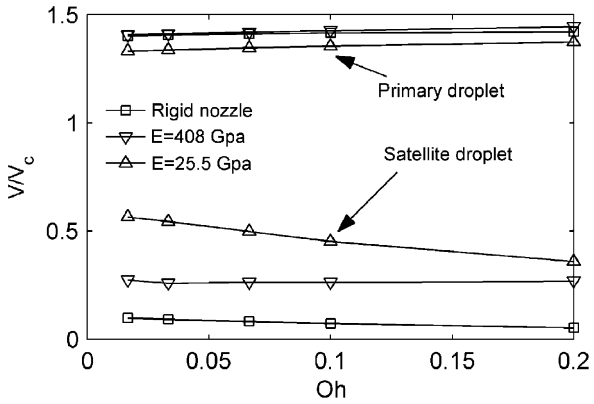

Fig. 9. Droplet volume after break-off, nondimensionalized by the capillary volume, $V_c = 4/3\rho a^3$, versus Oh, for a rigid nozzle plate and two flexible plates measured by Young's modulus, E; for all cases $M_i/M_c = 1.2$.

The effect of Oh number on the time required for micro-droplet formation and the time required for satellite break-off for the imposed pressure pulse waveform is shown in Fig. 8. As Oh increases the micro-droplet and satellite break-off times increase linearly. The plate vibration has no discernable effect on the micro-droplet or satellite formation time. Since it may be anticipated that the plate vibration would induce a certain level of perturbations to the ejected fluid column, and results show little sensitivity of break-off time with plate vibration, it can be concluded that these perturbations are either very weak, or of a time scale much longer than the flow effects induced by the pressure pulse driving the fluid ejection process. The satellite formation time is a fixed offset from the droplet formation time, with a value near $t_b/t_c = 0.5$. The break-off of satellites from the nozzle exit plane are largely controlled by the surface tension forces, which are dependent on the local liquid surface curvature at the nozzle exit plane. The nozzle vibration alters the curvature such that the deceleration caused by surface tension is reduced, resulting in longer break-off times.

The effect of nozzle vibration on the primary and satellite micro-droplet volume for the imposed pressure pulse waveform is shown in Fig. 9. The primary micro-droplet volume is only weakly affected by the nozzle vibration, where the most flexible plate, the lowest value of E, results in slightly smaller micro-droplet volumes. Based on this, a plate with a very low frequency and a high amplitude vibrational mode can potentially reduce the droplet volume. The nozzle vibration causes the satellite volume to increase, and the volume increment is dependent on the plate stiffness. The less stiff plate yields the largest satellite volume. As shown in Fig. 8, the vibrating nozzles take longer for satellite break-off. The longer break-off time results in more fluid leaving the nozzle forming the filament, which results in a larger satellite volume.

The satellite filament's shape, at the primary micro-droplet break-off, satellite break-off and satellite filament break-off, for a fluid with Oh = 0.0167 and 0.2, are shown in Fig. 10. It is seen that the satellite shape is dependent on both the nozzle vibration characteristics and the fluid viscosity. The break-off of the satellite filament is the combined effect of the contraction of the liquid filament and the development of the instabilities induced by nozzle vibration. For the vibrating nozzle case, the long liquid thread has a break-off which results in multiple satellite droplets when the fluid viscosity is low, Oh = 0.0167. But for the higher viscosity fluid, Oh = 0.2, the development of instabilities is resisted by the viscous effects. As a result, a smaller number of satellites are formed. The plate vibration characteristics affect the satellite break-off phase angle, which is discussed later in more detail. The satellite break-off phase angle affects the radius of the satellite filament, which in turn affects the number of satellites that are formed. A satellite break-off phase angle with backward movement of the nozzle, which occurs for the lower frequency low E values, results in a long liquid thread formation, shown in Fig. 10. While a satellite break-off phase angle with forward movement of the nozzle, at the higher frequency higher E values, results in a shorter liquid thread. The longer liquid thread that forms eventually breaks-off into multiple satellites, while the shorter liquid thread contracts to a single droplet before the instability causes the liquid thread to break-off.

The primary droplet and satellite velocities at the time of break-off, normalized by the capillary velocity, are shown in Fig. 11, as a function of the Oh number. Since the fluid velocity varies along the length of the droplet, and each grid element has a different volume, a mass weighted average velocity is used. Compared to the rigid nozzle case, vibration increases the droplet velocity by approximately the equivalent of the capillary velocity scale for all vibration cases presented. This increase is only a very weak function of the plate's Young's modulus, for the range of values studied. The reason for this large velocity increase is that the momentum of the nozzle is directly imparted to the local fluid

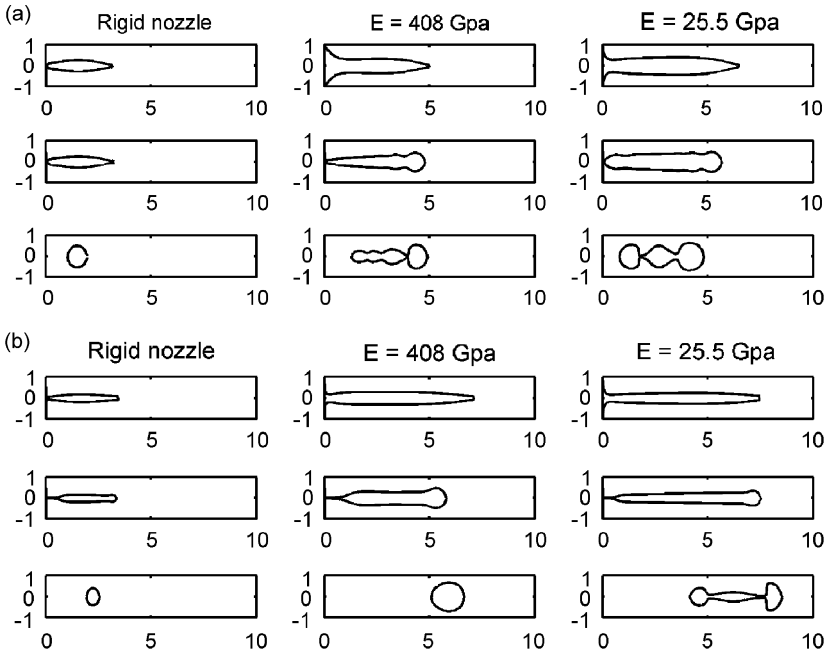

Fig. 10. Illustration of the droplet formation shapes at different times for a rigid nozzle plate and two flexible plates measured by Young's modulus, E; for all cases $M_i/M_c = 1.2$: (a) Oh = 0.0167 and (b) Oh = 0.2. All results are provided at the same relative times among cases.

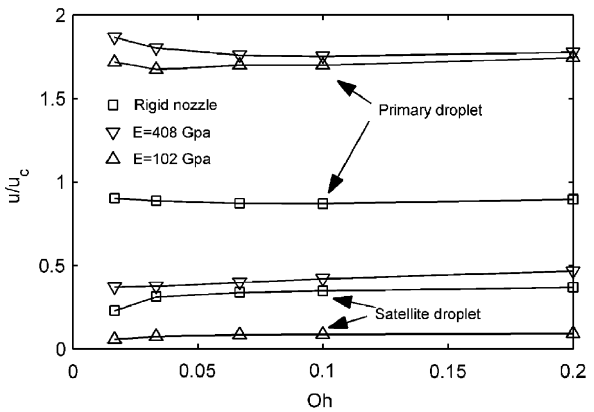

Fig. 11. Velocity of Primary and satellite droplets, nondimensionalized by the capillary velocity, versus Oh for a rigid nozzle plate and two flexible plates measured by Young's modulus, E; for all cases $M_i/M_c = 1.2$.

filament upon ejection. The break-off phase angle does not influence this increased momentum of the droplet. As can be inferred from Table 4, all of the plates have essentially the same initial acceleration. Consequently, the acceleration of the fluid first leaving the nozzle, which is the fluid that forms the primary droplet, determines the droplet momentum regardless of the relative phase of break-off. Therefore, it is the initial plate acceleration that is important in determining the observed increment of droplet velocity. The subsequent vibration amplitude and frequency of the plate do not significantly influence droplet momentum.

The satellite velocity is also represented as a mass weighted velocity, regardless of whether it eventually forms a single satellite droplet or multiple satellite droplets. The results in Fig. 11 indicate that the satellite velocity is dependent on the nozzle vibration characteristics, while the viscous effects, as expressed by Oh, only show a weak effect for the rigid case at the lower Oh value. For the cases studied, the nozzle vibration has a stronger affect on satellite velocity than the

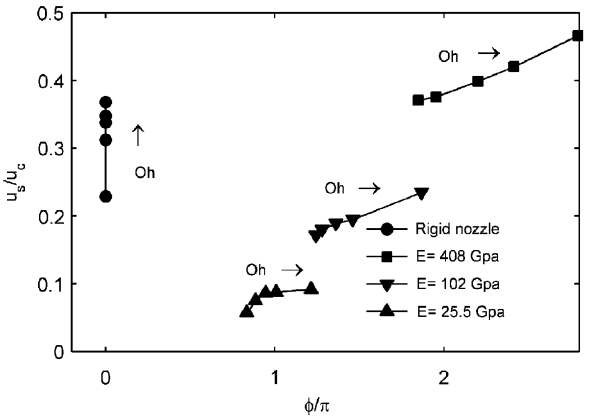

Fig. 12. Satellite velocity, nondimensionalized by the capillary velocity, versus nozzle vibration phase angle, normalized by π, for a rigid nozzle plate and three flexible plates measured by Young's modulus, E; for all cases $M_i/M_c = 1.2$; the rigid nozzle is shown at zero phase angle; the arrow indicates increasing value of Oh.

Table 4
Nozzle plate vibration characteristics, $P/P_c = 10$, $T/T_c = 0.12$

Young' modulus, E (GPa)	Vibration period, t_p/t_c	Peak deflection, $(w_0/a)_{\text{peak}}$	Peak velocity, $(u_0/u_c)_{\text{peak}}$	Initial acceleration, g_0/g_c
25.5	6.5000	1.4111	0.8212	6.8433
102	4.5600	0.9545	0.8209	6.8408
408	3.2500	0.6175	0.8195	6.8292

primary droplet velocity. This is because the satellite filament remains attached to the nozzle and the fluid velocity near the exit plane is directly affected by nozzle vibration. The stiffer plate with greater frequency of vibration results in somewhat larger velocities, which is thought to be a result of increased acceleration.

There is significant variation in the time history of the plate velocity and its acceleration as the plate stiffness changes. Results presented above indicate that the time of satellite break-off is not strongly dependent on the plate vibration; therefore, the satellite droplet formation will occur at different phases depending on the stiffness of the plate. Fig. 12 shows the mass weighted average satellite velocity versus phase angle at the time of satellite break-off. Note, that to indicate the rigid plate, these data are located at a phase angle of zero. Also, the arrow in the figure associated with each value of E indicates the direction of increasing Oh, which indicates increasing viscosity. Based on the relative phase of the satellite break-off, the stiffest plate has satellite break-off when the nozzle is advancing forward, therefore obtaining higher fluid velocities. Whereas the less stiff plates have satellite break-off when the nozzle is receding, and therefore have lower fluid velocities. Consequently, the relative phase, determined by the plate rigidity, strongly affects the satellite momentum after break-off. The only exception to this is the case of very high viscosity fluid (not shown) which results in a long thin filament attached to the nozzle which extends the break-off phase angle for $E = 102\,\text{GPa}$ to approximately 2π. This thin filament does not adversely reduce the satellite momentum since its mass is very low.

5. Conclusion

A numerical simulation for micro-droplet formation from a naturally vibrating nozzle is formulated. It is found that the nozzle vibration causes the primary micro-droplet velocity to increase significantly, while the primary micro-droplet break-off time and micro-droplet volume are only weakly affected by the nozzle vibration. The increase of the primary droplet velocity is closely related to the magnitude of the nozzle acceleration at the beginning of the pressure pulse, and is independent of the Young's modulus of the nozzle material. The more flexible nozzle plates result in significantly larger total satellite volume. The satellite velocity depends on the break-off phase relative to the nozzle vibration cycle. Results indicate that it may be possible to design a pressure pulse to deliver a droplet with a higher velocity while the

resultant filament flows back into the nozzle. Further study is needed to examine effects of variation of the pressure waveform on the droplet formation process in order to achieve a practical design for a high-speed droplet without satellite formation.

References

Adams, R.L., Roy, J., 1986. A 1-D numerical model of a drop-on-demand ink jet. Journal of Applied Mechanics 53, 193–197.

Ambravaneswaran, B., Wilkes, E.D., Basaran, O.A., 2002. Drop formation from a capillary tube: comparison of 1-D and 2-D analyses and occurrence of satellite drops. Physics of Fluids 14, 2606–2610.

Bogy, D.B., Talke, F.E., 1984. Experimental and theoretical study of wave propagation phenomenon in drop-on-demand ink jet devices. IBM Journal of Research and Development 28, 314–321.

Chen, A.U., Notz, P.K., Basaran, O.A., 2002. Computational and experimental analysis of pinch-off and scaling. Physical Review Letters 88, 1745011–1745014.

Day, R.F., Hinch, E.J., Lister, J.R., 1998. Self-similar capillary pinchoff of an inviscid fluid. Physical Review Letters 80, 704–707.

Eggers, J., 1993. Universal pinching of 3D axisymmetric free-surface flow. Physical Review Letters 71, 3458–3460.

Eggers, J., Dupont, T.F., 1994. Drop formation in a 1-D approximation of the Navier–Stokes equation. Journal of Fluid Mechanics 262, 205–221.

Elrod, S.A., Hadimioglu, B., Khuri-Yahub, B.T., Rawson, E.G., Richley, E., Quate, C.F., Mansour, N.N., Lundhren, T.S., 1989. Nozzleless droplet formation with focused acoustic beams. Journal of Applied Physics 65, 3441–3449.

Fromm, J.E., 1982. Numerical calculation of the fluid dynamics of drop-on-demand jets. IBM Journal of Research and Development 28, 322–333.

Kamisuki, S., Hagata, T., Tezuka, C., Nose, Y., Fuji, M., Atobe, M., 1998. A low power, small, electrostatically-driven commercial inkjet head. In: Proceedings of the 1998 IEEE Micro Electro Mechanical Systems, pp. 63–68.

Kamisuki, S., Fujii, M., Takekoshi, T., Tezuka, C., Atobe, M., 2000. A high resolution, electrostatically-driven commercial inkjet head. In: Proceedings of the 2000 IEEE Micro Electro Mechanical Systems, pp. 793–798.

Lin, S.P., 2003. Breakup of Liquid Sheets and Jets. Cambridge University Press, Cambridge, UK.

Middleman, S., 1995. Modeling of Axisymmetric Flow. Academic Press, New York.

Pan, F., Kubby, J., Chen, J., 2002. Numerical simulation of fluid-structure interaction in a MEMS diaphragm drop ejector. Journal of Micro-Mechanics and Micro-Engineering 12, 70–76.

Percin, G., Khuri-Yakub, B.T., 2003. Piezoelectric droplet ejector for ink-jet printing of fluids and solid particles. Review of Scientific Instruments 74, 1120–1127.

Peregrine, D.H., Shoker, G., Symon, A., 1990. The bifurcation of liquid bridges. Journal of Fluid Mechanics 212, 25–39.

Roman, M., Aubry, N., 2003. Design and fabrication of electrostatically actuated synthetic microjets. In: Proceedings of ASME IMECE2003, IMECE2003-41579.

Shield, T.W., Bogy, D.B., 1986. A numerical comparison of 1-D fluid jet models applied to drop-on-demand printing. Journal of Computational Physics 67, 327–347.

Shield, T.W., Bogy, D.B., Talke, F.E., 1987. Drop formation by DOD ink-jet nozzle: a comparison of experimental and numerical simulation. IBM Journal of Research and Development 31, 96–110.

Soedel, W., 1993. Vibrations of Shells and Plates. Marcel Dekker, New York.

Szilard, R., 1974. Theory and Analysis of Plates. Prentice-Hall, New Jersey.

Yamamoto, K., Kawashima, T., Watanabe, T., Tokunaga, T., 1991. Drop formation in a drop-on-demand ink jet. In: Yang, W.-C., Woods, R.L. (Eds.), Flucome '91: 3rd Triennial International Symposium on Fluid Control, Measurement, and Visualization, pp. 339–342.

Yang, G., 2003. A numerical model of drop-on-demand droplet formation from a vibrating nozzle and rigid nozzle. Master Thesis, Oregon State University, Corvallis, OR.